

Investigating the chemical composition of mixed organic–inorganic particles by “soft” vacuum ultraviolet photoionization: The reaction of ozone with anthracene on sodium chloride particles

Eric Gloaguen^a, Erin R. Mysak^b, Stephen R. Leone^{a,c}, Musahid Ahmed^a, Kevin R. Wilson^{a,*}

^a Chemical Sciences Division, Lawrence Berkeley National Laboratory, 1 Cyclotron Road, Berkeley, CA 94720, USA

^b Department of Chemistry, University of North Carolina, Chapel Hill, NC 27599, USA

^c Departments of Chemistry and Physics, University of California, Berkeley, CA 94720, USA

Received 28 April 2006; received in revised form 22 July 2006; accepted 26 July 2006

Available online 28 August 2006

Abstract

The ozone reaction with anthracene coated sodium chloride particles is measured by single photon ionization of the resulting volatilized gas phase molecules. To investigate in detail the organic fraction of particles, a vacuum ultraviolet aerosol mass spectrometer (VUV-AMS) has been developed at the Chemical Dynamics Beamline at the Advanced Light Source. This instrument combines a thermal vaporization particle source with tunable synchrotron radiation. Since VUV is a “soft” ionization method, the roles of both the vaporization and ionization steps on the fragmentation patterns of $C_{30}H_{62}$ hydrocarbons are observed. Conditions can be found to obtain mass spectra without significant fragmentation of the molecules. This technique is used to characterize the products of the heterogeneous reaction of gas phase ozone with particle phase anthracene on size-selected sodium chloride particles, conducted in a flow tube experiment. The recorded fragment-free mass spectra show several new products from mono- to penta-oxygenated anthracene. The kinetics of the product formation and particle size measurements are simultaneously recorded, revealing that an increase of the particle size accompanies the formation of the products.

© 2006 Elsevier B.V. All rights reserved.

Keywords: Aerosol; Heterogeneous reaction; Anthracene; Ozone; Single photon ionization

1. Introduction

Submicron aerosol particles are involved in many processes that impact tropospheric chemistry, climate, and human health. Experiments designed to probe the particle phase of aerosols are mainly used to evaluate the role of particulate matter in the radiative balance and heterogeneous chemistry of the troposphere. However, in general nanoparticles themselves are useful tools to study the physics of surfaces, heterogeneous chemistry or as new ways to introduce non-volatile or fragile material into the gas phase for spectroscopic analysis [1]. In any case, the complete chemical characterization of these nanoscale systems is crucial, but remains an outstanding challenge. Among the many aerosol properties now routinely quantified (e.g., number density, par-

ticle size distribution, morphology), the chemical composition, in particular the organic fraction, is very hard to determine.

Many techniques are used to identify molecules in the particle phase. Off-line measurements consist of collecting particles on filters for post-analysis using a suite of techniques now available in modern analytical chemistry laboratories [2]. However, modification of the sample composition during the various analysis steps is always of concern. Such changes make direct, real-time measurements preferable [3]. With the development of modern aerosol mass spectrometers (AMSs), detailed mass spectra can now be obtained on single particles or on ensembles, thus providing new ways to directly correlate the size of the particle with chemical composition [2].

AMSs are currently used by many groups [4] as broadly outlined in this issue, as well in a previous review by Sullivan and Prather [3]. The capability of these instruments to characterize the chemical composition of various particle types (e.g., inorganic or non-refractory) is mainly determined by the method

* Corresponding author. Tel.: +1 510 495 2474; fax: +1 510 486 5311.
E-mail address: krwilson@lbl.gov (K.R. Wilson).

of particle vaporization and subsequent ionization. For organic aerosols, new “soft” ionization methods are being developed to minimize the fragmentation in the particle mass spectra, thus yielding greater insight into the organic complexity and heterogeneous chemistry of tropospheric aerosol particles.

In general, molecules that comprise an aerosol particle are introduced into the gas phase either by laser ablation or desorption, or by thermal vaporization on a resistively heated surface. Energy deposited into the system by a laser can be controlled using two-color laser desorption ionization (LDI) or by matrix-assisted laser desorption ionization (MALDI) techniques [5]. The internal energy of molecules resulting from thermal vaporization can also be well controlled. For example, low temperature vaporization was found to reduce the internal energy of neutral molecules prior to ionization, thus reducing the degree of unwanted dissociative photoionization observed in the mass spectrum [1]. For techniques that employ hard ionization (e.g., laser ablation or 70 eV electron impact ionization), most of the fragmentation of organic molecules occurs during the ionization step itself, often masking the role of internal energy in the particle vaporization step.

Electron impact, chemical ionization and laser photoionization are ionization sources used in current AMSs [3]. Another complementary approach developed in our laboratory consists of coupling tunable vacuum ultraviolet (VUV) radiation with a thermal vaporization aerosol mass spectrometer (VUV-AMS). 7–30 eV VUV radiation is produced at the Chemical Dynamics Beamline of the Advanced Light Source (Lawrence Berkeley National Laboratory). Tunable VUV radiation allows one step threshold ionization for organic molecules, thereby greatly reducing the fragmentation [1] that is observed in most systems that are studied by electron impact or laser multi-photon ionization. This instrument was specifically designed as a soft ionization probe of the heterogeneous chemistry of laboratory simulated organic aerosol particles.

The performance of the VUV-AMS and its suitability to study submicron organic aerosol particles is illustrated with two examples. In Section 2, the first example reveals how internal energy in both the particle vaporization and ionization steps of long chain hydrocarbons ($C_{30}H_{62}$) influences fragmentation in mass spectra. In addition to controlling the fragmentation observed in particle mass spectra, tunable VUV also provides a way to distinguish between $C_{30}H_{62}$ isomers by ionization energy. These results could aid the design of new field-based single wavelength VUV photoionization aerosol mass spectrometers. The second example, in Section 3, illustrates how tunable VUV can be used to study the heterogeneous reaction of nanometer-sized sodium chloride particles coated with polyaromatic hydrocarbons (PAHs) with gas phase ozone.

2. VUV-AMS: “soft ionization” of thermally vaporized organic aerosol particles

2.1. Description of the VUV-AMS

The VUV-AMS used in this experiment has been described previously [1,6]. Briefly, aerosols are sampled into the vacuum

through a 200 μm aperture. The particle beam is focused by an aerodynamic lens [7], after which it passes into a differential pumping chamber through a 2 mm skimmer. The maximum transmission efficiency (~ 1) of the aerodynamic lens occurs for 70–800 nm diameter particles. The particle beam then enters the third detection chamber through a 4 mm skimmer where the particles are thermally vaporized on a heated 3 mm diameter copper tip located in between the repeller and accelerator grids. For the temperature and organic compounds presented in this paper, there is no evidence that molecules stick to the copper heater, suggesting that most of the particles hitting the tip are flash vaporized. The heater is positioned at ~ 3 mm from the extraction axis where tunable VUV light, produced by the Chemical Dynamics Beamline at the Advanced Light Source (Lawrence Berkeley National Laboratory) ionizes the molecules in the gas plume created by the vaporization of the particles. The photon energy is produced by an undulator with a spectral bandwidth of 2.5%. The undulator light passes through an argon gas filter and a MgF_2 window to remove residual high energy harmonic photons. Under these conditions, 7.7–11.2 eV photons are delivered at the VUV-AMS endstation at a nominal flux of 10^{16} photons s^{-1} . Ions are extracted by a set of time of flight (TOF) ion optics, which consist of three 16 mm equally spaced 7.62 cm diameter grids forming the repeller, accelerator and a ground electrode at the entrance of a 0.76 m field free region of the TOF mass spectrometer. Many different extraction techniques (voltages, pulse lengths, and sequences, etc.) were explored to optimize the sensitivity and resolution of the VUV-AMS. For the anthracene data shown in Section 3, the optimal configuration is as follows. A 2.00 kV dc bias voltage is applied to the heater and the repeller and accelerator electrodes. Ions are extracted by 4.7 μs pulses of 0.49 and 0.23 kV applied to the repeller electrode and heater, respectively. This configuration yields a resolution of $m/\Delta m = 10^3$, where Δm is the full width at half maximum (FWHM) of the $m/z = 210$ ion peak. Ions were collected on a dual chevron micro channel plate located at 0.81 m from the interaction region of the particle and photon beams. The TOF mass spectra are recorded at 28 kHz on a multichannel scaler with 8 ns bin width under normal operations. The experiments on $C_{30}H_{62}$ were recorded under different extraction conditions than those outlined above yielding slightly degraded mass resolution.

2.2. Control of fragmentation in the detection of long chain hydrocarbons

To illustrate both the main features of the VUV-AMS for the analysis of nanoparticle organic chemistry as well as some more fundamental aspects of the role of internal energy in aerosol mass spectrometry, the photoionization dynamics of long chain hydrocarbons were investigated. In particular, homogeneously nucleated nanometer-sized particles were prepared by passing 0.5 L min^{-1} dry nitrogen through a heated (373–423 K) glass vessel containing one of two $C_{30}H_{62}$ isomers. The resulting particle size distribution is somewhat broad (FWHM = 250 nm) with a mean diameter of 300 nm.

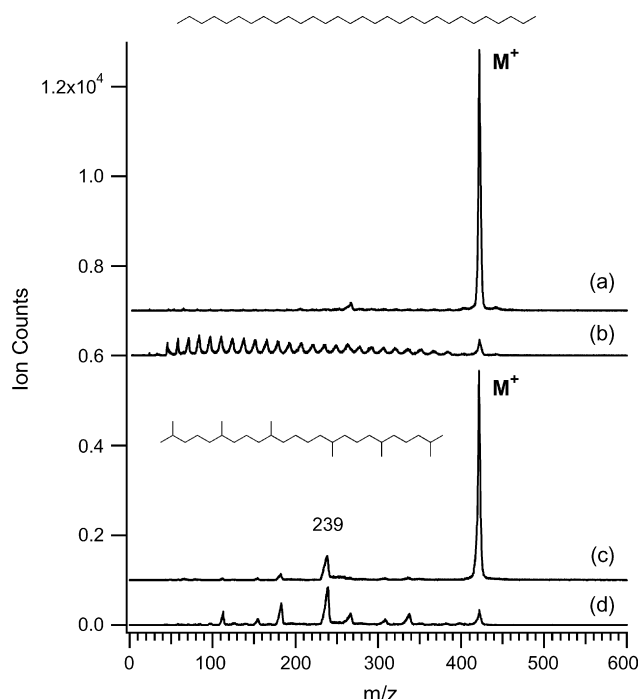


Fig. 1. 10.7 eV photoionization mass spectra of $C_{30}H_{62}$ at various particle vaporization temperatures: triacontane at (a) 373 K and (b) 698 K and squalane at (c) 373 K and (d) 673 K.

Shown in Fig. 1 are 10.7 eV photoionization particle mass spectra of two isomers of $C_{30}H_{62}$, the linear chain triacontane and the branched hydrocarbon squalane. At a particle vaporization temperature of 373 K the mass spectra (Figs. 1(a) and (c)) of molecules volatilized from solid triacontane and liquid squalane, respectively, are nearly identical, fragment-free and dominated by the molecular ion peak at $m/z = 422$. As the heater temperature is increased, at a fixed ionization energy of 10.7 eV, the differences between these two isomers become easily discernable in Figs. 1(b) and (d).

At high temperatures the triacontane particle mass spectrum exhibits a fragmentation pattern dominated by sequential CH_2 elimination typical of a linear hydrocarbon chain. In contrast, a more complex mass spectrum is observed for squalane resulting from fragmentation of the cation at various branch sites. Since

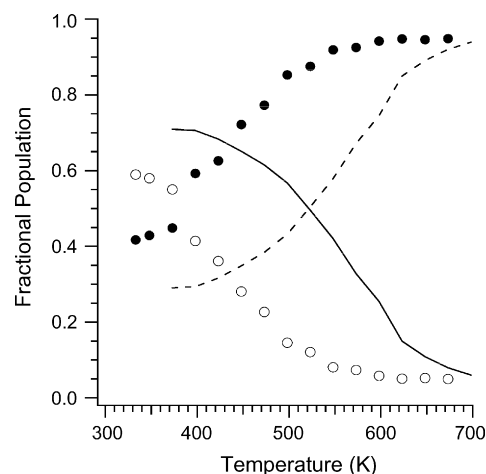


Fig. 2. 10.7 eV temperature-dependent fractional populations: squalane parent ion (\circ), squalane fragment ions (\bullet), triacontane parent ion (—), triacontane fragment ions (---). Populations were obtained by integrating peak areas.

the photoionization energy is fixed for all the spectra shown in Fig. 1, the changes in fragmentation behavior are entirely due to changes in internal energy of the neutral molecule during the particle vaporization step. This increase in internal excitation of the neutral molecule is thus manifested in the mass spectrum through more efficient dissociative photoionization.

Fig. 2 shows how the fractional populations of the parent molecular ion and total integrated fragment signal depend explicitly upon particle vaporization temperature. At 10.7 eV ionization energy, both triacontane and squalane molecular ions dominate at low temperatures with 60–70% of the total spectral intensity. At temperatures in excess of 500 K, the fragments dominate the photoionization mass spectrum. For squalane, the populations of parent and fragment ions are nearly equal at 380 K, while the equivalence point in triacontane is shifted to 500 K. This is apparently due to the partitioning of thermal energy into the different vibrational or rotational states of a branched versus linear hydrocarbon cation. In addition, a very small contribution is due to photoionizing these molecules at slightly different energies above threshold.

The ionization energy of these isomers can be obtained by tuning the photon energy and recording the appearance of the

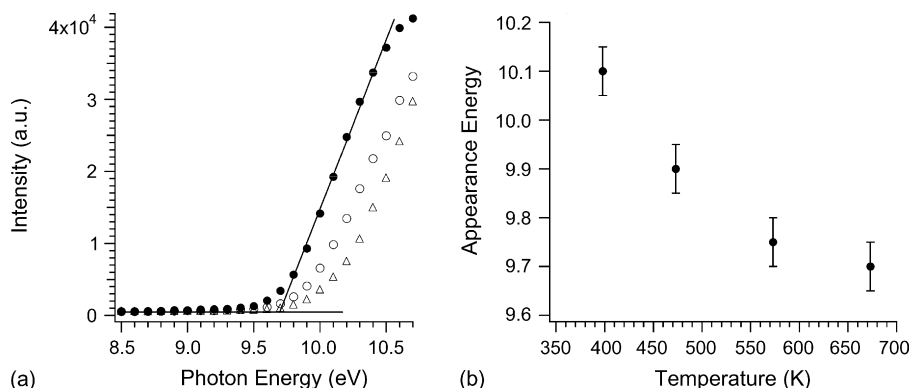


Fig. 3. (a) Photoionization efficiency curves for squalane: (\bullet) $m/z = 422$ and (Δ) $m/z = 239$ at $T = 398$ K and (\circ) $m/z = 239$ at $T = 473$ K. (b) Shift in appearance energy of $m/z = 239$ with increasing temperature.

molecular ion peak ($m/z=422$). The ionization energy can be determined from a linear fit of the photoionization efficiency (PIE) curves shown in Fig. 3(a) for squalane. The ionization energy of triacontane is 10.0 ± 0.1 eV. In contrast, the ionization onset of squalane is measured to be 9.7 ± 0.1 eV. Photoionization at high photon energies shows that harder ionization of organic molecules such as these yields mass spectra dominated by small mass fragmentation patterns. For example, during 70 eV electron ionization of these gas phase molecules, a considerable amount of internal excitation (~ 60 eV) is deposited into internal vibrational or rotational modes of the cation that efficiently couple to fragmentation of the molecular ion.

In general, the differences in isomer ionization energies provide an additional tool to unravel complex particle mass spectra. For example, this approach has been used to distinguish isomers and overlapping masses in the photoionization mass spectra of complex systems such as flames [8]. In Section 3, PIE measurements will be used to assign the various oxidation products of anthracene. In general, identifying isomeric products can yield new insight into mechanisms of heterogeneous particle phase chemistry.

Also shown in Fig. 3(a) is the PIE curve measured at a particle vaporization temperature of 300 K for the $m/z=239$ fragment of squalane. The appearance energy of this ion is 0.4 eV above the parent molecular ion at 10.1 ± 0.1 eV. It should be noted that all of the fragments in the squalane mass spectra shown in Fig. 1 exhibit similar onset energies. As the particle vaporization temperature is increased, the appearance energy of the $m/z=239$ fragment undergoes a corresponding shift to lower energy. Given the resolution of our experiment the ionization energy (not shown) of the molecular ion $m/z=422$ is observed to be independent of vaporization temperature (9.7 eV) consistent with previous results indicating that the ionization cross section of a neutral molecule is minimally affected by an increase in internal energy. As the particle vaporization temperature is further increased to 600 K the appearance energy of the fragment becomes nearly coincident with the ionization onset of the parent molecular ion. This shift in appearance energy clearly demonstrates that thermal excitation of the neutral molecule couples into the dissociative modes of the molecular ion at lower photon energies. The temperature dependent shift in appearance energy of $m/z=239$ is shown explicitly in Fig. 3(b) and is discussed in detail by us in a recent study of biological particle photoionization mass spectrometry [1].

Fig. 4 summarizes the contribution of both the vaporization and ionization steps to the fragmentation dynamics of squalane. It shows how the fractional population of the molecular ion depends upon both the heater temperature and ionizing wavelength. To achieve a fragment-free mass spectrum, low heater temperatures and threshold photon energies should be utilized to minimize the dissociative ionization by reducing unwanted internal excitation in either the neutral molecule or cation. In other words, the vaporization temperature is used to shift the fragment appearance energies to higher photon energies. Conversely, higher temperatures or photon energies allow a more detailed assignment of the parent molecular ion through the analysis of unique photoionization fragmentation

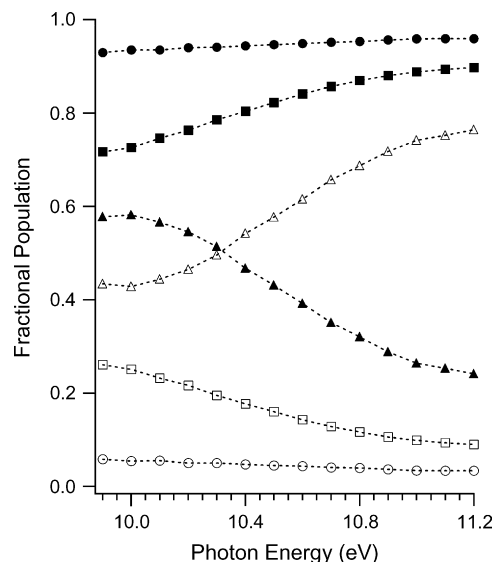


Fig. 4. Fractional population of the molecular (solid symbols) and fragment (open symbols) ions of squalane as a function of photon energy at various particle vaporization temperatures: (●) 398 K, (■) 473 K and (▲) 573 K.

patterns (e.g., linear versus branched hydrocarbons) shown in Fig. 1.

To take full advantage of the chemical specificity of mass spectrometry for the analysis of organic aerosol particles, fragmentation of the molecular ion should be minimized. Using the tunable “soft” ionization technique described here allows more detailed insight into the role of internal energy (and therefore fragmentation in mass spectra) during the particle vaporization step. In particular, these results show that the particle vaporization temperature exerts considerable influence on the degree of mass spectral fragmentation. These thermal effects are often obscured by other more “hard” ionization techniques. These results could be useful in optimizing the wavelength and vaporization temperature of new field-based fixed wavelength VUV instruments in order to target specific molecules or particle types in the troposphere. For laboratory-based experiments, tunable VUV provides a way to distinguish between isomers or overlapping masses, necessary to understand the more subtle mechanistic details of heterogeneous particle phase chemistry of aerosol proxies. In the next section, many of the tools described here will be applied to a more atmospherically relevant example: the oxidation of anthracene by ozone.

3. Heterogeneous chemistry of anthracene

PAHs are pollutants resulting from incomplete combustion. Emitted mainly by many human activities [9], these contaminants are present in the atmosphere partitioned between the gas and particle phase, in the soil, and in ground water. Since these molecules and their oxidation products are suspected of having a negative impact on human health [10], oxidation reactions of PAHs are currently the subject of intense study. However, particle phase reactivity still remains one of the least understood processes. Nanometer-sized particles behave like micro-reactors

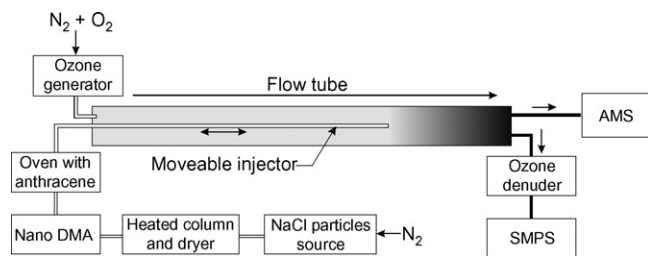


Fig. 5. Schematic of the experimental setup.

producing new molecules, which can be directly assimilated by organisms during respiration. Such chemistry is investigated in this paper through the heterogeneous reaction between particle phase anthracene and gas phase ozone. The difficulty of characterizing products in such a gas-surface reaction is illustrated by the recent paper of Kwamena and coworkers [11] who were the first to quantify one product, 9,10-anthraquinone, of this heterogeneous reaction between ozone and anthracene.

Our approach consists of first coating size-selected sodium chloride particles with anthracene, after which the kinetics of the heterogeneous reaction with ozone is monitored in a flow tube reactor. Such mixed particles, consisting of an inorganic core surrounded by an organic layer, represent a common structural motif of many particles detected in the troposphere [12]. One of the main advantages of this technique is that size-selection allows fine control over the amount of anthracene deposited in the particle phase, thus allowing the investigation of changes in particle size resulting from the reaction. To accomplish this, the particle size distribution and concentration were recorded by a Scanning Mobility Particle Sizer (SMPS), while changes in chemical composition were simultaneously probed by the VUV-AMS.

3.1. Experimental

3.1.1. Experimental design

Sodium chloride particles are produced by either atomizing a 2.0 g L^{-1} ($3.4 \times 10^{-2} \text{ mol L}^{-1}$) aqueous solution (TSI, model no. 3076) or nebulizing a 0.5 g L^{-1} ($0.9 \times 10^{-2} \text{ mol L}^{-1}$) aqueous solution (Artistic Delights, mist maker fogger). These methods produce broad size distributions with a mean diameter of 75 and 155 nm, respectively, and total particle concentrations at the output of the dryer (see below) between $\sim 3 \times 10^7$ and $8 \times 10^6 \text{ particles cm}^{-3}$, respectively. Particles are transported from the source via dry nitrogen at a flow rate set at 0.35 L min^{-1} .

The polydisperse particle distribution was sent through a stainless steel column heated to $\sim 110^\circ\text{C}$ (see Fig. 5) and a room temperature diffusion dryer using blue silica gel desiccant. The relative humidity of the aerosol flow exiting the diffusion dryer was measured to be less than 5% (Traceable[®] Hygrometer, Fisher Scientific). Size-selected particles were extracted from the polydisperse distribution using a differential mobility analyzer (TSI electrostatic classifier, model 3080; impactor with 0.071 cm orifice; nano-DMA, TSI model 3085; bipolar charger ^{85}Kr). Size-selected sodium chloride particles were then sent through an oven (Carbolite, TZF 12/38/400) containing a 45 cm

long, 3 cm inner diameter Pyrex tube containing solid anthracene (Aldrich, 95%). The temperature of the oven could be adjusted so that controlled amounts of anthracene were deposited on the NaCl particles (Section 3.2). NaCl particles coated with anthracene were finally sent to the moveable injector input of a flow tube. Conductive silicone tubing (TSI), to minimize wall loss, was used to transport the particles.

Ozone was produced by sending a 3:1 mixture of dry nitrogen and dry air into a commercial ozone generator (Ozone Services, Yanco Industries Ltd., model 0580K). Metastable nitrogen could also be produced in the generator. However, AMS and SMPS measurements have been checked to be dependent on ozone only. The output flow, carried in Teflon tubing, was sent to the sheath input of the flow tube at a rate of 0.4 L min^{-1} . The ozone generator was set to deliver an ozone concentration of 77 ppm (Ozone Monitor, 2B Technologies Inc., model 202M) in the sheath flow, leading to a concentration of 44 ppm ($\sim 1.2 \times 10^{15} \text{ molecules cm}^{-3}$) after mixing with particles coated with anthracene and before reaction.

The flow tube (Fig. 5) consists of a 110 cm length and 25.4 mm inner diameter Pyrex tube with a 125 cm length, 4.3 mm inner diameter and 6.3 mm outer diameter moveable Pyrex injector. The design and the settings of the experiment ensure laminar flow ($Re < 200$): the mixing of the reactants is then mainly due to the diffusion of the reactants. Complete mixing of the reactants is estimated to be completed within the first 10 cm after the tip of the injector. As a result, only data taken in the 10–90 cm range will be considered. These distances correspond to 4–36 s reaction times. The total flow exiting the flow tube is 0.75 L min^{-1} and is sampled by both a Scanning Mobility Particle Sizer (SMPS) (0.25 L min^{-1}) and the VUV-AMS (0.27 L min^{-1}). The excess flow not sampled by either instrument is simply exhausted.

The SMPS consists of a differential mobility analyzer (TSI electrostatic classifier, model 3080; impactor with 0.071 cm orifice; long DMA, TSI model 3081; bipolar charger ^{85}Kr) coupled to a condensation particle counter (CPC, TSI model 3025 A). The fraction of the flow sent to the SMPS first passes through an ozone denuder (Carulite 200, Carus Chemical). This denuder is located as close as possible from the end of the flow tube to remove ozone and thus stop the reaction between anthracene and ozone as quickly as possible. The time needed for the particles to travel from the flow tube to the denuder is about $\sim 0.5 \text{ s}$. This then ensures that the particle concentration as a function of particle mobility diameter measured by the SMPS reflects the state of the system at the end of the flow tube. Connections between the flow tube and the SMPS are made with conductive silicone tubing (TSI).

The VUV-AMS sampling aperture (Section 2.1) is co-located near the SMPS sampling region at the end of the flow tube. As the reaction is stopped when particles enter vacuum, the data taken with the VUV-AMS to chemically characterize the particles can be directly correlated with the SMPS data on the time scale of 1 s. Vaporization temperatures in excess of 150°C did not significantly increase ($<10\%$) the overall ion signal. This temperature was thus selected to ensure quasi-complete vaporization of anthracene from the particles, and low enough to

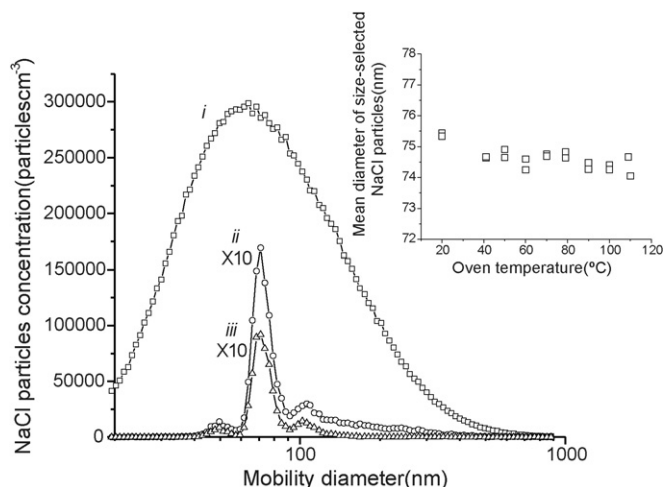


Fig. 6. NaCl particle size distribution: (i) polydisperse particle beam; (ii) size-selected particles after the nano-DMA; (iii) size-selected particles after the empty oven at room temperature, so no anthracene is deposited. The y-axis represents the number of particles in the interval $[d_i, d_{i+1}]$ with $\log(d_{i+1}/d_i) = 1/64$ where d_i is the mean mobility diameter measured by the SMPS. The inset shows the measured mean diameter of 63.8 nm size-selected sodium chloride particles as a function of empty oven temperature. This mean diameter of the non-coated particles is measured to be greater than 74 nm, which is due to both an imperfect calibration of the two DMAs, and the presence of larger particles going through the nano-DMA (see text).

reduce fragmentation during photoionization [1] as discussed above in Section 2.2.

3.1.2. NaCl seed particle characterization

To fully characterize the particles, their size distribution was measured with the SMPS at different locations in the experimental setup (see Fig. 6): (i) after the dryer to characterize the polydisperse particles (atomizer source), (ii) after the nano-DMA to characterize the size-selected particles (selected size: 63.8 nm), and (iii) after the oven without anthracene. The mobility diameters in this paper will be interpreted as the theoretical volume equivalent diameter which is defined as the diameter of a spherical particle having the same volume as the particle for which the mobility diameter has been measured.

The profile measured at (ii) consists of one main peak at 71 nm due mainly to singly charged particles having the size of interest, and two satellite peaks on both sides of the main peak. The slight difference between the selected size and the measured size arises from the imperfect calibration of the two DMAs, but does not affect the relative size measurements made in this work. The two satellites at 50 and 106 nm are assigned, respectively to 71 nm doubly charged particles, and 106 nm singly charged particles [13,14].

The size-selected particles are not perfectly monodisperse. However, depending on what portion of the polydisperse particle beam distribution is selected, 60–90% of the particles are the size of interest. Consequently, the comparison with profile (i) shows that the nano-DMA is able to extract ~7% of the 71 nm diameter particles from the original polydisperse distribution.

From a comparison of profiles (ii) and (iii), the transmission efficiency of monodisperse particles through the empty oven (anthracene removed) at room temperature is determined to be 50%. In addition, the particle profile remains unchanged by the oven within the accuracy of the measurement. To examine whether the oven temperature influences the non-coated sodium chloride particles, the particle size distribution was measured as a function of increasing oven temperature. No significant change in either particle number or size distribution was observed. The mean mobility particle diameter (Fig. 6) reflects the stability of the sodium chloride particles at oven temperatures between 20 and 110 °C. The dispersion in the measurements yielded a 0.8 nm absolute error in the mean mobility diameter. This absolute error was also found for the other size-selected particle measurements reported here and is in agreement with the theoretical accuracy of the Tandem DMA (TDMA) technique [15].

3.1.3. Anthracene coating

With the behavior of pure NaCl aerosols well characterized, the deposition of anthracene on these particles is studied by two sets of experiments. To examine the thickness dependence of anthracene on the seed particles, several anthracene deposition oven temperatures were investigated. First, the nano-DMA was set to select 30 nm diameter NaCl particles. The particle size distribution and the anthracene ion counts were recorded simultaneously, in the absence of ozone, as a function of increasing

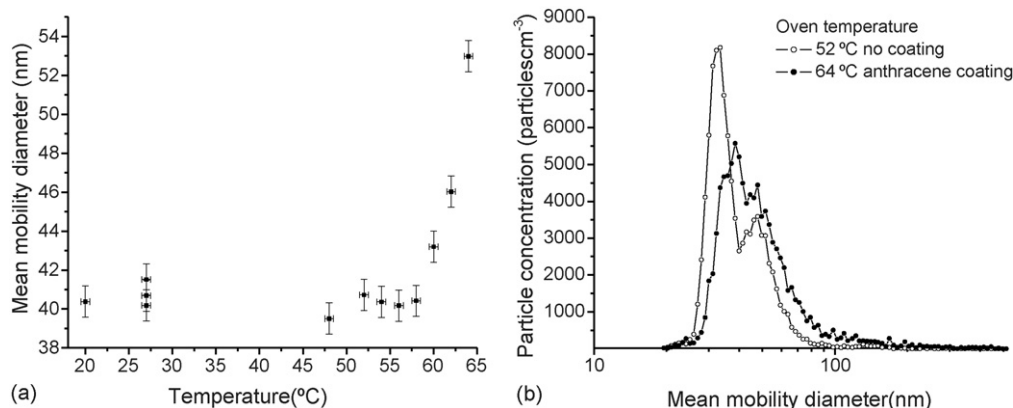


Fig. 7. Characterization of the anthracene coating. (a) Evolution of the mean mobility diameter as a function of the oven temperature. (b) Size distribution of size-selected sodium chloride particles before coating (oven temperature 52 °C) and after anthracene coating (oven temperature 64 °C).

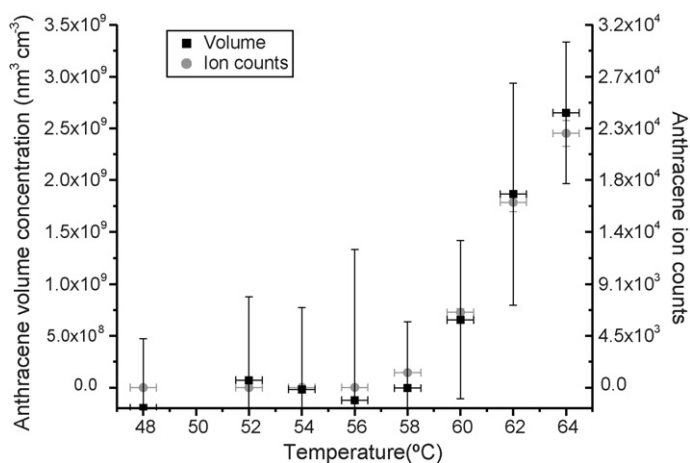


Fig. 8. SMPS and VUV-AMS measurements of the anthracene coating. Comparison between the anthracene volume concentration (see text) and the anthracene ion counts (integrated anthracene peak of mass spectra recorded during 10 s). Error bars on the volume are from the uncertainty of the particle diameter measurement, and those for ion counts are estimated by examining the fluctuation of signal for a given temperature (relative error of 5%).

oven temperature while the molecules were ionized by 10.7 eV light.

The mean mobility diameter measured by the SMPS is shown in Fig. 7(a). It clearly shows an increase in particle diameter whereas the particle concentration shows no significant variations (not shown). In order to rule out homogenous nucleation of anthracene in the oven, a filter was placed before the oven to remove NaCl particles. No particle signal was detected when this filter was in place. Since the transmission of NaCl particles through the empty oven produced no obvious shift in particle size (Section 3.2), the increase in diameter is due to an anthracene coating on the NaCl particles. The coating observed in Fig. 7(b) is not a simple shift to larger diameter, but includes a slight broadening of the size-distribution. However, the size distribution of coated particles is still reasonably monodisperse when compared to the non-coated profile. Hence, the mean mobility diameter is thus a parameter that characterizes the coating of individual particles quite well.

TOF mass spectra reveal the presence of anthracene at oven temperatures in excess of 58 °C. Here again, a filter was placed before the oven thus removing the NaCl seed particles. Under these conditions no anthracene ions were detected, clearly indicating that the observed ion signal originates from an anthracene coating on a NaCl particle and not from either pure homogeneously nucleated anthracene particles or from the transmission of anthracene vapor from the oven through the aerodynamic lens. The evolution of this ion signal as a function of the oven temperature is shown in Fig. 8.

The quasi-complete vaporization of anthracene on the particles ensures that the amount of anthracene detected by the VUV-AMS is proportional to the total amount of anthracene deposited on the particles. Assuming the density of the coating is homogeneous and identical for all the oven temperatures investigated, the ion signal is then proportional to the volume of deposited anthracene. The volume concentration, v_{ant} , for one oven temperature, T , can be calculated knowing the mean diam-

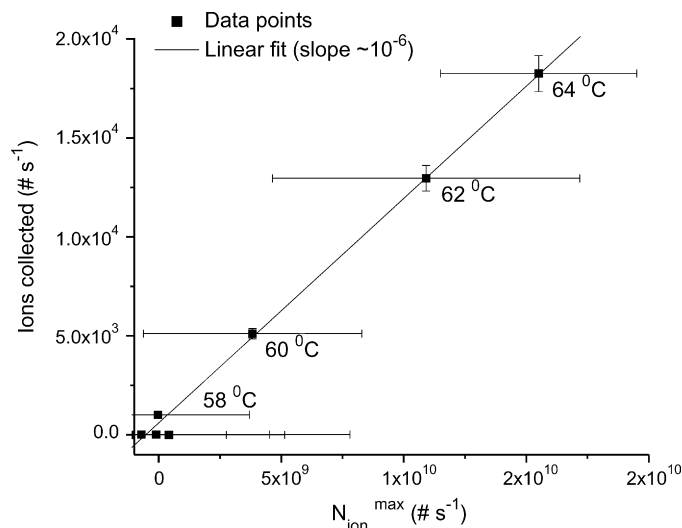


Fig. 9. Detection sensitivity of the VUV-AMS instrument. A linear regression based on the method of the least squares has been performed to fit the data points. The slope calculated at $(1.13 \pm 0.04) \times 10^{-6}$ characterizes the sensitivity of the VUV-AMS.

eter of particles, d , the mean diameter of non-coated particles, d_{nc} , the particle concentration, n_p , and by assuming the particles are spherical:

$$v_{\text{ant}}(T) = n_p(T) \frac{\pi(d^3(T) - d_{\text{nc}}^3)}{6} \quad (1)$$

This last assumption is reasonable since the non-coated 30 nm sodium chloride particles are possibly nearly spherical as discussed by Zelenyuk and coworkers [13]. d_{nc} is an average value of the diameter of uncoated NaCl particles measured between 20 and 56 °C. The comparison between the volume of anthracene deposited on the particles and the ion counts shows a good agreement (see Fig. 8) between both data sets.

It is also possible to quantify the detection sensitivity of the VUV-AMS by comparing the theoretical maximum number of ions collected per unit of time, $N_{\text{ion}}^{\text{max}}$ versus the number of ions detected. $N_{\text{ion}}^{\text{max}}$ is calculated using the following formula:

$$N_{\text{ion}}^{\text{max}}(T) = \frac{\gamma_{\text{Ant}}^{10.7 \text{ eV}} N_A \rho_{\text{Ant}} v_{\text{Ant}}(T) \phi}{M_{\text{Ant}}} \quad (2)$$

where M_{Ant} is the molecular weight of anthracene (178.23 g mol⁻¹), $\gamma_{\text{Ant}}^{10.7 \text{ eV}}$ is the anthracene ion quantum yield at 10.7 eV (0.3 according to Jochims and coworkers [16]), N_A is Avogadro's number, ρ_{Ant} is the volumetric mass of anthracene (1.283 g cm⁻³ [17]) and ϕ is the volumetric flow rate at the inlet of the VUV-AMS (0.27 L min⁻¹). This theoretical maximum ion number assumes that all anthracene molecules entering the VUV-AMS are photoexcited, and it takes into account the ionization efficiency of anthracene at 10.7 eV, while assuming 100% ion collection efficiency. Both theoretical and measured ion yields are plotted in Fig. 9 for oven temperatures between 48 and 64 °C. From these data, the detection efficiency of our instrument is estimated to be approximately 10⁻⁶ ions per molecule (the variation of the transmission efficiency of the aerodynamic lens due to the increase in particle size is neglected here). This sensitiv-

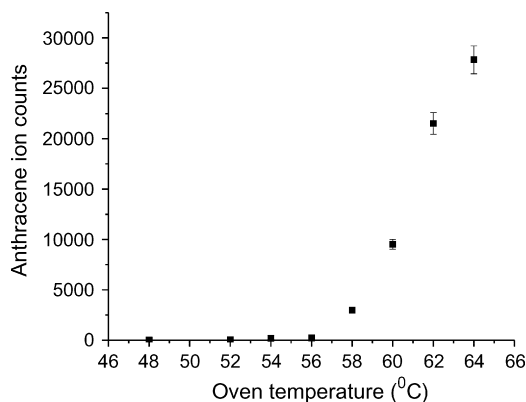


Fig. 10. Detection by the VUV-AMS of 70 nm size-selected particles coated with anthracene at several oven temperatures. SMPS measurements allow for a correlation of the VUV-AMS ion signal detected at 64 °C with an average anthracene coating of 1.1 nm. As the SMPS cannot measure a thinner coating, the thickness has been estimated from VUV-AMS data to be 0.4 nm at 60 °C (see text).

ity is similar to that reported for other AMSs using the electron impact technique [18,19].

To illustrate this sensitivity, an anthracene coating of 70 nm particles (diameter close to the maximum of the particle size distribution (Fig. 6) giving a particle concentration of 2.0×10^5 particles cm^{-3}) was also investigated. The AMS data (see Fig. 10) show an increase of the anthracene ion signal as a function of the oven temperature. The number of ions detected at 64 °C can be correlated with a coating of $(1.1 \pm 0.8$ nm) radial thickness measured with the SMPS. This thickness is close to the thinnest measurable by the SMPS, but Fig. 10 also shows that the VUV-AMS is able to detect anthracene on these particles at lower temperatures, thus corresponding to an even thinner coating than that which is measurable by the SMPS. At 60 °C, this radial thickness is estimated from the ratio of ion counts to be 0.4 ± 0.3 nm or ~ 1 anthracene monolayer [20,21].

3.2. Results and discussion

To study the reaction between ozone and the coated particles, coating parameters were chosen to maximize the amount

of anthracene on the particles in order to produce measurable changes in both the SMPS and VUV-AMS data. 150 nm size-selected NaCl particles were produced by the nebulizer. The mean mobility diameter for these particles was measured to be 195 ± 0.8 nm. The particles were then coated with a 14 nm thick anthracene layer (anthracene oven temperature set at 65 °C, mean mobility diameter measured to be 223 ± 0.8 nm). This amount of anthracene in the particle phase leads to a concentration of $\sim 10^{12}$ molecules cm^{-3} . The particles were then exposed to 44 ppm ozone ($\sim 1.2 \times 10^{15}$ molecules cm^{-3}) and the condensed phase products analyzed by the VUV-AMS and SMPS.

3.2.1. Product identification

To identify the products of the reaction between ozone and anthracene, mass spectra were recorded at 10.7 eV. For these measurements, the injector position was kept at a fixed position corresponding to a reaction time of 36 s. Several reaction products (see Fig. 11) were identified at $m/z = 193$, **194**, 195, 197, **208**, 209, **210**, 211, 224, 225, **226**, 227, 334 (bold numbers are for the four most intense signals). To check the origin of these products, a filter was placed between the flow tube and the AMS to confirm that these products originate from the particle phase. In addition, a filter was placed before the oven to confirm that products are not coming from any particles produced by the reaction. PIE curves are obtained by recording the ion signal of each m/z as a function of photon energy (see examples in Fig. 12). The photon energy, selected by the undulator, is calibrated by using the known PIE curve of benzene. Mainly two kinds of PIE curves were obtained. The first (type a) exhibits only one well-defined slope from which the photoionization energy of the molecule can be extracted by fitting a line through the ionization onset. The second type of PIE curve (type b) exhibits a more complicated multi-linear behavior that suggests the presence of at least two isomers with different ionization energies. From these curves two extreme photoionization energies can be obtained, corresponding to the two isomers with the highest and lowest ionization energy (IE). Some products giving the most intense signal have been tentatively assigned using both the molecular weight and photoionization energies (or electron impact IEs when photoionization energies data are not available) [22] of compounds reported in Table 1.

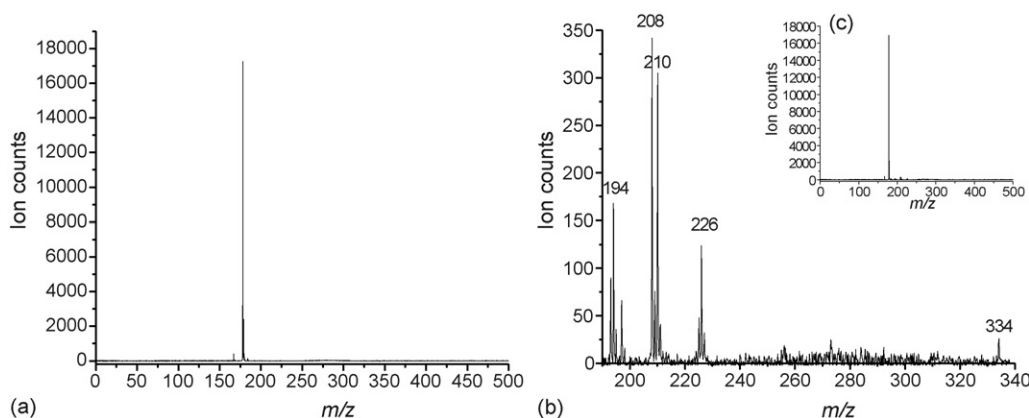


Fig. 11. (a) Mass spectrum of anthracene. (b) Mass spectrum of the products of the reaction between ozone and anthracene. This spectrum is the difference between spectra recorded when the ozone generator was on (c) and off (a). All spectra have an acquisition time of 10 s.

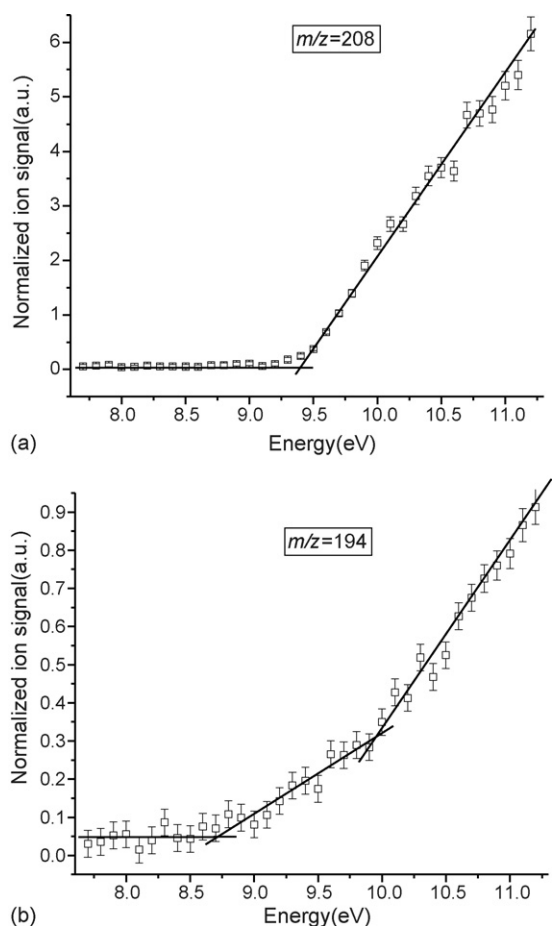


Fig. 12. Photoionization efficiency curves of ions of $m/z = 208$ (a) and 194 (b). For both, peaks from the mass spectra are integrated and normalized by the intensity of the synchrotron beam.

The most intense product at $m/z = 208$ has an IE of 9.4 ± 0.1 eV (see Fig. 12(a)). This m/z can correspond to several di-oxygenated anthracene isomers. The IE measurement allows us to determine which isomers agree with the observations; for example, 9,10-anthraquinone (9.25 ± 0.03 eV) agrees with the observed results, whereas 1,4-anthraquinone (8.45 ± 0.2 eV) does not agree (Table 1). The former is the most likely to be produced in our experiment, as 9,10-anthraquinone had been indeed previously detected as the main product of ozonation of anthracene in solution [23], at an air-aqueous interface [24], and for anthracene adsorbed on Pyrex tubes [11]. Other more highly oxidized products such as phthalic acid [11,23] or naphthalenedicarboxylic acid [23] have also been reported, but were not observed in our experiments. This disparity could arise most likely due to the different reaction and detection conditions employed in this work.

The PIE curve recorded for the ion of $m/z = 194$ is shown in Fig. 12(b). The shape of the curve suggests that more than one species is detected at this value of m/z , which corresponds to a mono-oxygenated anthracene molecule. Such molecules have not been previously detected as products of the heterogeneous reaction between anthracene and ozone [11,24]. The IEs of 1-hydroxyanthracene and 2-hydroxyanthracene (7.7 eV) are not compatible with the range of product IEs detected (8.7–9.9 eV).

However, anthrone (8.8 eV) could be the isomer detected with the lower IE. Furthermore, this molecule has been proposed by Bailey and coworkers [23] as an intermediate leading to the formation of 9,10-anthraquinone in solution. The other isomer with the higher IE might be 9,10-dihydro-9,10-epoxyanthracene but an unambiguous determination cannot be made as the IE for this species is currently unknown.

The lack of IE data on di-oxygenated and tri-oxygenated anthracene molecules ($m/z = 210$ and 226) also does not allow for precise assignments. However, given the trend of IEs of benzenediols compared to phenol, di- and tri-hydroxyanthracene are expected to have IEs lower than the IE of mono-hydroxyanthracene (7.7 eV) and are therefore not good candidates. It is also possible to compare the IEs of di-oxygenated and tri-oxygenated anthracene with the mono-oxygenated anthracene molecules. Given that anthrone has an IE of 8.8 eV, mono- and di-hydroxyanthrone are expected to have a lower IE, which is consistent with the lower limit measured at 8.6 and 8.3 eV for ions of $m/z = 210$ and 226. 9,10-endoperoxideanthracene or dibenz[*b,e*]oxepin-11(6H)-one can fit for high IE isomers at $m/z = 210$. 9,10-endoperoxideanthracene and hydroxyanthrone have both been characterized previously as photo-oxidation products of anthracene on a dry surface [25].

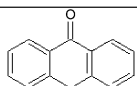
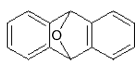
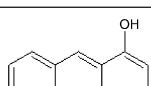
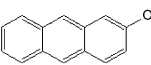
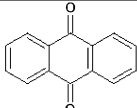
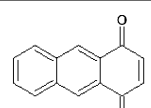
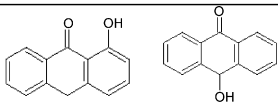
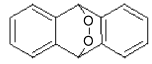
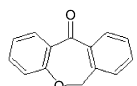
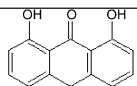
At longer TOF accumulation times, ions of higher m/z (240, 242, 256) were also detected. They are consistent with tetra- and penta-oxygenated compounds. Unfortunately, the signal was too weak to fully characterize them through their PIEs. These highly oxygenated (tri- and higher) molecules are believed to be photo-oxidation products of anthracene [26]. However, it seems that under the conditions of our experiment, without specific light exposure, such products are formed. The identification of these particle phase products is particularly interesting as they have proven to have a dramatically enhanced toxicity compared to anthracene [10].

Longer TOF accumulation times also revealed several ions with $m/z > 300$. These ions can be products, or fragments of products having higher masses, as the PIE of ions of $m/z = 334$ is the only one which does not fit a type a or b curve (Fig. 12), and it might show evidence of fragmentation at an ionization energy above 9.7 eV. In any case, the observation of these ions of high m/z suggests that at least dimerization could occur during the oxidation process. Particles may then have a complex chemistry even after a relatively short (<1 min) reaction time. However, the observation of the fragment-free dimerization product of $m/z = 334$ between 8.7 and 9.7 eV indicates that VUV-AMS is a powerful technique to study oligomerization in the particle phase, and the results can provide deeper insights into atmospherically relevant chemistry [27].

3.2.2. Kinetics

Different reaction times (from 4 to 36 s) were investigated by changing the injector position. The photon energy was kept at 10.7 eV. The evolution of the ion signal as a function of reaction time was recorded for all the products. Unfortunately the corresponding measurement for anthracene proved difficult due to fluctuations of the parent signal in the mass spectra. How-

Table 1
IEs of products and their possible assignments

m/z	IEs measured from the PIEs (eV) ± 0.1 eV	Possible molecules IE (eV) [22]	Molecules not possible IE (eV) [22]
193	8.8–9.7 ^a		
194	8.7–9.9 ^a	 anthrone $8.83^a \pm 0.03$ 9.43^b  9,10-dihydro-9,10-epoxyanthracene	 1-hydroxyanthracene 7.70^b  2-hydroxyanthracene 7.73^b
195	8.9 ^a		
197	9.1 ^a		
208	9.4 ^a	 9,10-anthraquinone $9.25^a \pm 0.03$ $9.4^b \pm 0.08$	 1,4-anthraquinone $8.45^a \pm 0.02$
209	9.2 ^a		
210	8.6–9.6 ^a	 hydroxyanthrones < 8.8  9,10-endoperoxideanthracene  dibenz[b,e]oxepin-11(6H)-one 9.63^b	dihydroxyanthracene < 7.7
211	9.1 ^a		
224	9.1–10.2 ^a		
225	9.2–10.6 ^a		
226	8.3–9.5 ^a	 dihydroxyanthrones < 8.8	trihydroxyanthracene < 7.7
227	9.3 ^a		
334	8.7 ^a		

^aPhotoionization. ^bElectron impact.

ever, anthracene was detected even at the longest reaction time indicating that the reaction with ozone did not consume all the anthracene molecules on the particles.

The kinetics of 9,10-anthraquinone formation is shown in Fig. 13(a). The amount of product increases linearly as a function of the reaction time. Such a linear increase has also been found for the formation of all the main products mentioned previously. This behavior is characteristic of a pseudo zero order reaction for the formation of these products, meaning that the rate coefficient apparently does not depend on both ozone and

anthracene concentrations. This result is consistent with the pseudo first order anthracene decay reported by Kwamena and coworkers [11] and Mmereki and Donaldson [28]. In that study, the ozone concentrations are similar to those used in this work ($\sim 10^{15}$ molecules cm^{-3}) but the reaction time investigated was much larger than the timescale investigated here (< 36 s).

The reaction has also been investigated by increasing the ozone concentration by a factor of 2 ($\sim 2.4 \times 10^{15}$ molecules cm^{-3}). No change in the products or formation rates ($< 5\%$) were observed by the VUV-AMS, confirming that the

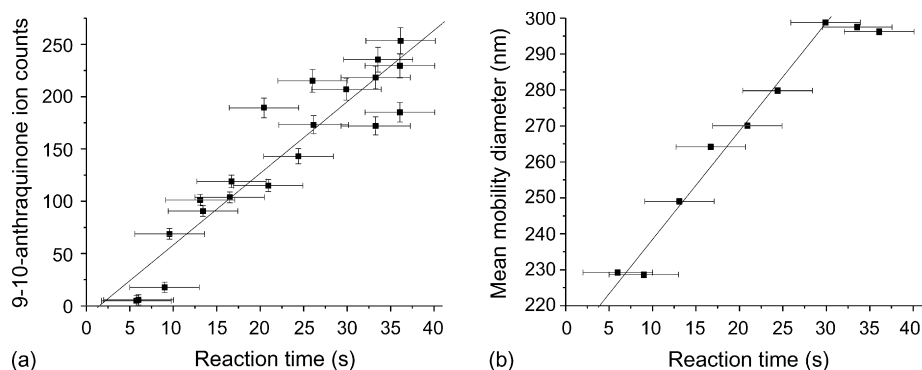


Fig. 13. Product kinetics. (a) 9,10-Antraquinone ion counts are reported here after integration of the corresponding peak on the mass spectra measured at different injector positions. The uncertainty of the mixing time between reactants leads to an estimated absolute error in reaction time of 4 s. (b) Particle size evolution as a function of reaction time. A linear regression based on the method of least squares has been performed excluding the two last data points. The slope of the resulting line is $3 \pm 1 \text{ nm s}^{-1}$.

rate constants observed here are not dependent on ozone concentration. This insensitivity with respect to these ozone concentrations has also been found by Kwamena and coworkers [11]. Their study at several ozone concentrations is in agreement with a Langmuir–Hinshelwood reaction mechanism [11,28,29]. This model describes the stability of the product formation rate as a function of ozone concentration due to saturation of the adsorption sites by ozone molecules. This saturation occurs when the following condition is fulfilled

$$K_{\text{O}_3}[\text{O}_3] \gg 1 \quad (3)$$

where K_{O_3} is the adsorption equilibrium constant. According to our measurements at $[\text{O}_3]_1 = 1.2 \times 10^{15} \text{ molecules cm}^{-3}$ and $[\text{O}_3]_2 = 2.4 \times 10^{15} \text{ molecules cm}^{-3}$, K_{O_3} must then be larger than $1/[\text{O}_3]_1 \approx 8 \times 10^{-16} \text{ cm}^3$. As the NaCl particles are coated on average by 36 layers of anthracene, it is most likely that this lower limit of the adsorption equilibrium constant reflects ozone partitioning directly onto anthracene rather than on sodium chloride. Even in the hypothesis of a non-complete coverage of the particles by anthracene, the case of ozone partitioning on sodium chloride appears also unlikely as it has been characterized [30] by an equilibrium constant lower than $1.2 \times 10^{-16} \text{ cm}^3$. Ozone could also partition onto the Pyrex flow tube according to the value found by Kwamena and coworkers [11] $((2.8 \pm 0.9) \times 10^{-15} \text{ cm}^3)$. However, the authors [11] could not exclude the possibility that ozone may partition onto anthracene in their system, and we believe a reaction occurring on Pyrex is unlikely to be detected in our experiment since the VUV-AMS is directly probing the reaction products on the particles themselves (Section 3.2.1).

Particle size measurements have been simultaneously recorded by the SMPS to monitor changes in particle size or concentration as a function of the reaction time. The mean particle diameter shows a linear increase of $3 \pm 1 \text{ nm s}^{-1}$ (Fig. 13(b)) to reach a plateau at 297 nm. This increase corresponds to a growth of the total particle diameter by a factor of 1.33. The ozone generator was turned off to check that this increase of the particle size could indeed be assigned to a chemical reaction. In addition, no particles are detected in the presence of ozone without the

anthracene coated particles, confirming that particles were not formed by secondary gas phase reactions or by reactions with tubing walls.

This increase in particle diameter that accompanies anthracene oxidation can be due to several processes such as a significant decrease in particle density, or a change in water uptake ability of the particles. Further experiments investigating the role of RH, the relative amount of particle constituents and their chemical composition are thus in progress to understand the growth mechanism observed during the reaction. These points will be discussed in detail in a forthcoming paper.

4. Conclusion

This paper demonstrates that VUV-AMS is a powerful way to record fragment-free particle mass spectra when combined with thermal vaporization and single photon ionization. Thermal vaporization allows fine control of the amount of internal energy imparted to systems such as long chain hydrocarbons. In addition, the sensitivity of this technique allows for the detection of a monolayer of organic material deposited on inorganic particles. As it has been demonstrated recently that polypeptides can be detected through fragment-free mass spectra [1], new biologically related fields [31], like nanophase biomolecule-solvent or enzyme substrate spectroscopies then become accessible with this technique.

VUV-AMS has also proven to be a useful tool to study the heterogeneous reaction of particle phase anthracene with gas phase ozone. The acquisition of fragment-free mass spectra allowed the characterization of several new reaction products through their IEs. However, unambiguous assignment of various isomers is limited by the lack of data on the IEs of the possible products. Simultaneous measurements by VUV-AMS and the SMPS have revealed a correlation between the formation of oxidation products and a dramatic increase in the particle size; the mechanism, however, remains unclear. Further investigations examining coating thickness, RH dependences and chemical nature of the particle constituents are in progress to determine the respective roles of the organic layer and the inorganic core

in this change in particle diameter. The results of these studies will have important implications for chemistry induced changes in particle size, as it has the potential to impact light scattering and cloud formation in the troposphere [32–34].

Acknowledgments

This work was supported by the Director, Office of Energy Research, Office of Basic Energy Sciences, Chemical Sciences Division of the US Department of Energy under contract no. DE-AC02-05CH11231.

References

- [1] K.R. Wilson, M. Jimenez-Cruz, C. Nicolas, L. Belau, S.R. Leone, M. Ahmed, *J. Phys. Chem. A* 110 (2006) 2106.
- [2] M.F. Sipin, S.A. Guazzotti, K.A. Prather, *Anal. Chem.* 75 (2003) 2929.
- [3] R.C. Sullivan, K.A. Prather, *Anal. Chem.* 77 (2005) 3861.
- [4] J.-L. Jimenez, <http://cires.colorado.edu/~jjose/ams.html>, 2006.
- [5] A.L. Hunt, G.A. Petrucci, *Trends Anal. Chem.* 21 (2002) 74.
- [6] J. Shu, K.R. Wilson, M. Ahmed, S.R. Leone, *Rev. Scient. Instrum.* 77 (2006) 43106.
- [7] X. Zhang, K.A. Smith, D.R. Wornsnop, J.-L. Jimenez, J.T. Jayne, C.E. Kolb, J. Morris, P. Davidovits, *Aerosol Sci. Technol.* 38 (2004) 619.
- [8] C.A. Taatjes, S.J. Klippenstein, N. Hansen, J.A. Miller, T.A. Cool, J. Wang, M.E. Law, P.R. Westmoreland, *Phys. Chem. Chem. Phys.* 7 (2005) 806.
- [9] B.J. Finlayson-Pitts, J.-N. Pitts Jr., *Science* 276 (1997) 1045.
- [10] A. Mallakin, B.J. McConkey, G. Miao, B. McKibben, V. Snieckus, D.G. Dixon, B.M. Greenberg, *Ecotoxicol. Environ. Saf.* 43 (1999) 204.
- [11] N.-O.A. Kwamena, M.E. Earp, C.J. Young, J.P.D. Abbatt, *J. Phys. Chem. A* 110 (2006) 3638.
- [12] D.J. Donaldson, V. Vaida, *Chem. Rev.* 106 (2006) 1445.
- [13] A. Zelenyuk, Y. Cai, D. Imre, *Aerosol Sci. Technol.* 40 (2005) 197.
- [14] K.J. Higgins, H. Jung, D.B. Kittelson, J.T. Roberts, M.R. Zachariah, *J. Phys. Chem. A* 106 (2002) 96.
- [15] D.J. Rader, P.H. McMurphy, *J. Aerosol Sci.* 17 (1986) 771.
- [16] H.W. Jochims, H. Baumgärtel, S. Leach, *Astron. Astrophys.* 314 (1996) 1003.
- [17] D.R. Lide, *Handbook of Chemistry and Physics*, 71st ed., CRC Press, 1991.
- [18] F. Drewnick, S.S. Hings, P. DeCarlo, J.T. Jayne, M. Gonin, K. Fuhrer, S. Weimer, J.L. Jimenez, K.L. Demerjian, S. Borrmann, D.R. Wornsnop, *Aerosol Sci. Technol.* 39 (2005) 637.
- [19] J.T. Jayne, D.C. Leard, X. Zhang, P. Davidovits, K.A. Smith, C.E. Kolb, D.R. Wornsnop, *Aerosol Sci. Technol.* 33 (2000) 49.
- [20] R. Niessner, P. Wilbring, *Anal. Chem.* 61 (1989) 708.
- [21] NIST, <http://ois.nist.gov/pah/>, 2006.
- [22] NIST, <http://webbook.nist.gov/chemistry/>, 2006.
- [23] P.S. Bailey, P. Kolsaker, B. Sinha, J.B. Ashton, F. Dobinson, J.E. Batterbee, *J. Org. Chem.* 29 (1964) 1400.
- [24] B.T. Mmerekki, D.J. Donaldson, J.B. Gilman, T.L. Eliason, V. Vaida, *Atmos. Environ.* 38 (2004) 6091.
- [25] R. Dabestani, K.J. Ellis, M.E. Sigman, *J. Photochem. Photobiol. A: Chem.* 86 (1995) 231.
- [26] A. Mallakin, D.G. Dixon, B.M. Greenberg, *Chemosphere* 40 (2000) 1435.
- [27] U. Baltensperger, M. Kalberer, J. Dommen, D. Paulsen, M.R. Alfarra, H. Coe, R. Fisseha, A. Gascho, M. Gysel, S. Nyeki, M. Sax, M. Steinbacher, A.S.H. Prevot, S. Sjögren, E. Weingartner, R. Zenobi, *Faraday Discuss.* 130 (2005) 265.
- [28] B.T. Mmerekki, D.J. Donaldson, *J. Phys. Chem. A* 107 (2003) 11038.
- [29] U. Pöschl, T. Letzel, C. Schauer, R. Niessner, *J. Phys. Chem. A* 105 (2001) 4029.
- [30] N.-O.A. Kwamena, J.A. Thornton, J.P.D. Abbatt, *J. Phys. Chem. A* 108 (2004) 11626.
- [31] T.S. Zwier, *J. Phys. Chem. A* 105 (2001) 8827.
- [32] M.C. Facchini, M. Mircea, S. Fuzzi, R.J. Charlson, *Nature* 401 (1999) 257.
- [33] M.D. King, K.C. Thompson, A.D. Ward, *J. Am. Chem. Soc.* 126 (2004) 16710.
- [34] J. Sun, P.A. Ariya, *Atmos. Environ.* 40 (2006) 795.